Dynamic superresolution by Bayesian nonparametric image processing

Ioannis Sgouralis[1], Ameya P. Jalihal[2], Lance W.Q. Xu (徐伟青)[3,4], Nils G. Walter[2], and Steve Pressé[3,4,5,*]

[1]Department of Mathematics, University of Tennessee, Knoxville, TN 37996, USA
[2]Single Molecule Analysis Group and Center for RNA Biomedicine, Department of Chemistry, University of Michigan, Ann Arbor, MI 48109, USA
[3]Center for Biological Physics, Arizona State University, Tempe, AZ 85287, USA
[4]Department of Physics, Arizona State University, Tempe, AZ 85287, USA
[5]School of Molecular Sciences, Arizona State University, Tempe, AZ 85287, USA
[*]Corresponding author (email: spresse@asu.edu)

Abstract

Assessing dynamic processes at single molecule scales is key toward capturing life at the level of its molecular actors. Widefield superresolution methods, such as STORM, PALM, and PAINT, provide nanoscale localization accuracy, even when distances between fluorescently labeled single molecules ("emitters") fall below light's diffraction limit. However, as these superresolution methods rely on rare photophysical events to distinguish emitters from both each other and background, they are largely limited to static samples. In contrast, here we leverage spatiotemporal correlations of dynamic widefield imaging data to extend superresolution to simultaneous multiple emitter tracking without relying on photodynamics even as emitter distances from one another fall below their diffraction limit. We simultaneously determine emitter numbers and their tracks (localization and linking) with the same localization accuracy per frame in regimes where widefield superresolution does for immobilized emitters ($\approx$50 nm). We demonstrate our results for both *in cellulo* data and, for benchmarking purposes, on synthetic data. To this end, we avoid the existing tracking paradigm relying on completely or partially separating the tasks of emitter number determination, localization of each emitter, and linking emitter positions across frames. Instead, we develop a fully joint posterior distribution over the quantities of interest, including emitter tracks and their total, otherwise unknown, number within the Bayesian nonparametric paradigm. Our posterior quantifies the full uncertainty over emitter numbers and their associated tracks propagated from origins including shot and camera artefact, pixelation, stochastic background, and out-of-focus motion. It remains accurate in more crowded regimes where alternative tracking tools do not apply.

Keywords: Fluorescence microscopy, Superresolution microscopy, Nanoscopy, Single molecule tracking, Image analysis, Bayesian nonparametrics

Introduction

Characterizing macromolecular assembly kinetics [6], quantifying intracellular biomolecular motility [41, 21, 22], or interrogating pairwise biomolecular interactions [47] requires accurate decoding of spatiotemporal processes at the single molecule level, *i.e.*, high, nm spatial and rapid, often ms, temporal scales. These tasks ideally require superresolving positions of dynamic targets, typically fluorescently labeled molecules (light emitters), to tens of nanometer spatial resolution [32, 52, 2] and, when more than one target is involved, discriminating between signals from multiple targets simultaneously.

Assessments by means of fluorescence experiments at the required scales suffer from inherent limitations. Such limitations often arise from the diffraction limit of light, $\approx 250\,\text{nm}$ in the visible range, below which conventional fluorescence techniques cannot achieve sufficient contrast between neighboring emitters of interest. To go beyond the limitations of conventional tools and achieve superresolution, contrast can be created through structured illumination [14], structured detection [24, 56, 55, 38], the photoresponse of fluorophore labels to excitation light [32, 52, 2, 45], or combinations thereof [17, 30, 57, 1].

Here we focus on widefield superresolution microscopy (SRM), which typically relies on fluorophore photodynamics to achieve superresolution. SRM is regularly used both *in vitro* [46, 25] and *in cellulo* [52, 2, 19, 51, 29, 37]. Specific widefield SRM image acquisition protocols, such as STORM [45], PALM [2], and PAINT [46], through their associated image analyses, decode positions of light emitters separated by distances below the diffraction limit, often down to the resolution of tens of nanometers [45, 2]. These widefield SRM protocols can be broken down into three conceptual steps: (i) specimen preparation; (ii) imaging; and (iii) computational processing of the acquired images (frames). The success of Step (iii) is ensured by both Steps (i)-(ii). In particular, in Step (i) engineered fluorophores are selected that enable the desired photodynamics; *e.g.*, photoswitching in STORM [45], photo-activation/bleaching in PALM [2], or fluorophore binding/unbinding in PAINT [46]. Step (ii) is then performed over extended periods, while awaiting rare photophysical (or binding-unbinding) events to manifest and for sufficient photons to be collected to achieve superresolved localizations in Step (iii). For well-isolated bright spots, Step (iii) achieves superresolved localization [27, 32, 52] while accounting for effects such as light diffraction, resulting in spot sizes of roughly twice $0.61\lambda/\text{NA}$ (the Rayleigh diffraction limit), set by the emitter wavelength (λ), the numerical aperture (NA) of the microscope's objective [43], the camera and its photon shot noise and spot pixelization.

In our work, we show that computation can be used to overcome both reliance on photophysics in Step (i) and for a long acquisition time in Step (ii), which not only limit widefield SRM largely to spatiotemporally fixed samples, but can also induce sample photodamage. In fact, while a moving emitter's distribution, or smearing, of its photon budget over multiple frames and pixels is a disadvantage in the implementation of Step (iii) above, we demonstrate - conversely - that such a distribution of the photon budget in both space and time provides information that can be leveraged to superresolve emitter tracks, determine emitter numbers, and help discriminate targets from their neighbors, even in the complete absence of photophysical processes (fig. 1).

Although captured in more detail in the framework put forward in the METHODS and expanded upon in a companion manuscript, here, we briefly highlight how our tracking framework, Bayesian nonparametrics (BNP)-Track, is fundamentally different from conventional tracking tools that determine emitter numbers, localize emitters, and link emitter locations as sequential steps. In the language of Bayesian statistics, resolving emitter tracks as well as emitter numbers amounts to constructing the probability distribution, $\mathbb{P}\left(\text{links}, \text{locations}, \text{emitter numbers}|\text{data}\right)$, which reads as "the joint posterior probability distribution of emitter numbers, locations, and links given a dataset". The best set of emitter number and tracks are those globally maximizing this probability distribution. Without further approximation, Bayes' theorem allows us to decompose this probability distribution as this product:

$$\begin{aligned}&\mathbb{P}\left(\text{links}, \text{locations}, \text{emitter numbers}|\text{data}\right)\\&= \mathbb{P}\left(\text{links}|\text{locations}, \text{emitter numbers}, \text{data}\right)\mathbb{P}\left(\text{locations}|\text{emitter numbers}, \text{data}\right)\mathbb{P}\left(\text{emitter numbers}|\text{data}\right). \quad (1)\end{aligned}$$

Single particle tracking tools that perform emitter number determination, emitter localization, and linking in separate steps invariably approximate the maximization of the joint distribution as a serial maximization of three terms. This process often involves additional approximations, such as using $\mathbb{P}\left(\text{links}|\text{locations}\right)$ to approximate $\mathbb{P}\left(\text{links}|\text{locations}, \text{emitter numbers}, \text{data}\right)$. Approximations such as these are acceptable for well-isolated and in-focus emitters, though they have fundamentally limited our ability to superresolve emitters especially as they move closer than light's diffraction limit. In contrast, BNP-Track avoids all such approximations and leverages all sources of information through the joint posterior to draw samples as well as maximize the posterior probability distribution, yielding superresolved emitter tracks.

The overall input to BNP-Track, includes both raw image sequences and known information on the imaging system, including the microscope optics and camera electronics as further detailed in METHODS. Using Bayesian nonparametrics, we provide a means of estimating unknowns including the number of emitters and their associated tracks. We demonstrate BNP-Track on experimental single particle tracking data, detailing how the simultaneous determination of emitter numbers and tracks can be computationally achieved. We also benchmark BNP-Track's performance against a well-established diffraction-limited tracking tool (TrackMate) to which we must confer some advantage (as direct comparison is not possible since existing tools do not simultaneously learn emitter numbers and associated tracks). More detailed comparisons are presented in the companion manuscript.

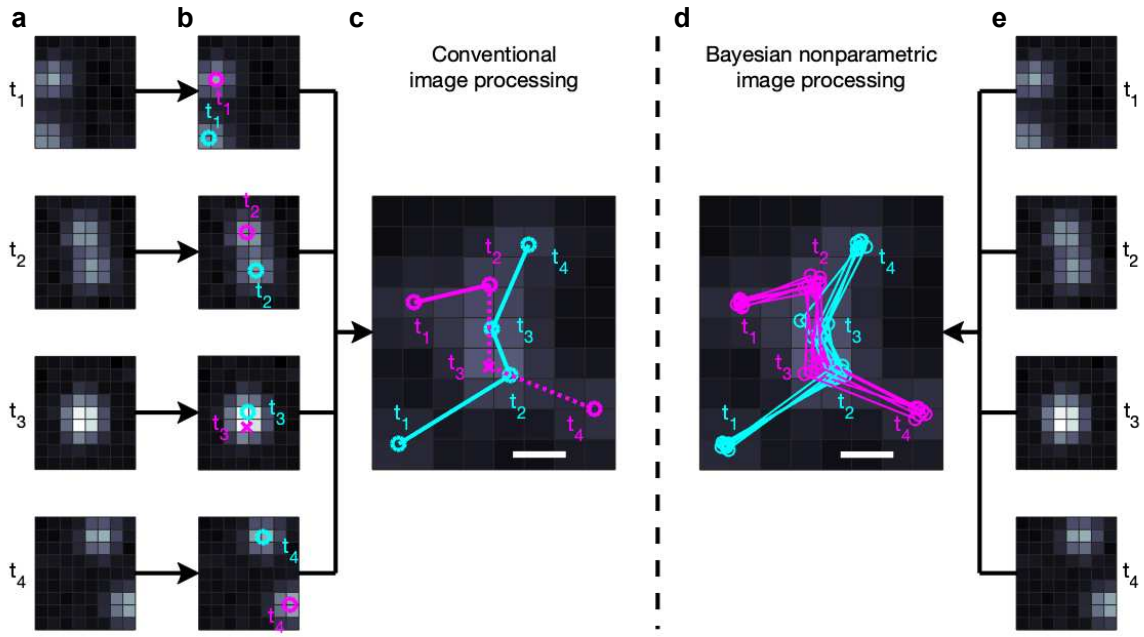

Figure 1: *Conceptual comparison between widely available tracking frameworks and BNP-Track.* **a** *and* **e**, *Four frames from a dataset showing two emitters.* **b**, *Existing tracking approaches [48, 23, 59, 34, 4, 58, 7, 13, 33, 60, 20, 3] either completely or partially separate the task of first identifying and then localizing light emitters in the field of view of each frame independently.* **c**, *Conventional approaches then link emitter positions across frames.* **d**, *Our nonparametric approach (BNP-Track) simultaneously determines the number of emitters, localizes them and links their positions across frames. In* **b-d**, *circles denote correctly identified emitters, and crosses denote missed emitters. In* **c** *and* **d**, *scale bars indicate a distance equal to the nominal diffraction limit given by the Rayleigh diffraction limit* $0.61\lambda/NA$.

Results

To demonstrate our BNP-Track analysis approach, we first analyze single mRNA molecules diffusing in live U-2 OS cells imaged under single-plane HILO illumination [49] on a fluorescence microscope as previously described [41, 39, 8], but using a beamsplitter to divide the single-color signal onto two cameras (figs. 2 and 3). The dual-camera setup allows us to test for consistency of BNP-Track's emitter number and track determination across cameras. In subsequent tests, we employ noise-overlaid synthetic data for which ground truth is known [48, 5] (figs. 4 and 5), and finally challenge BNP-Track with experimental data of crowded emitters (fig. 6).

As emitters evolve in 3D, it is possible, indeed helpful in more accurate lateral localization, for BNP-Track to estimate emitter axial distance ($|z|$) from the focal plane from 2D images using the width of the emitter's point spread function (PSF) sensitive to axial distance [61]. For this reason, while axial distance from the focal plane is always less accurately determined than lateral positions, we nonetheless report BNP-Track's axial estimates for experimental data in figs. 2 and 3 and, for synthetic data in figs. 5 and 6, compare our axial distance to the ground truth.

As tracking tools, such as TrackMate [48], do not estimate axial locations or emitter numbers, direct head-to-head comparison to other tracking tools is not possible and, for this reason, a detailed comparison of BNP-Track to augmented tracking tools is relegated to a companion manuscript alongside detailed robustness analysis of BNP-Track with detailed discussion of how both motion aliasing and stochastic background is treated. For completeness, however, in figs. 5 and 6 we provide an approximate comparison of BNP-Track to TrackMate.

Prior to showing results of BNP-Track, an important note on Bayesian inference is warranted. Developed within the Bayesian paradigm [50, 12, 53], BNP-Track not only provides point estimates over unknown quantities of interest, such as numbers of emitters and their associated tracks, but also distributions over them, which includes uncertainty. As we cannot easily visualize the output of multidimensional posteriors over all candidate emitter numbers and associated tracks, we often report estimates for emitters which coincide with the number of emitters which maximize the posterior termed *maximum a posteriori* (MAP) point estimates. Then, having determined the MAP number of emitters, we collect their associated tracks in figures such as figs. 2 to 4.

BNP-Track superresolves sparse single-emitter tracks in cellulo

No ground truth is known for tracks from experimental single particle tracking data. For this reason, we employed two separate camera cameras behind a beamsplitter. Following image registration due to unavoidable camera misalignment, this allowed us to independently process two datasets for subsequent comparison and error estimation knowing that, in principle, both cameras should have the same ground truth tracks though the noise realizations on both cameras is different.

In figs. 2a and 2b, we show, for illustrative purposes alone, time averages of a sequence of 22 successive frames spanning ≈ 2.5 s of real time in both detection channels. In the data processing, we analyze the underlying frames without averaging. All raw data are provided in the SUPPORTING INFORMATION.

From these frames, we track well separated or dilute emitters, *i.e.*, having their PSFs always be well separated in space, in a $5\,\mu$m wide square region of interest (ROI), named ROI-1. Figure 2a also zooms in on ROI-1. The BNP-Track derived track estimates are shown in fig. 2c while, in fig. 2e, all samples from the posterior are superposed. As, due to fundamental optical limitations, we cannot determine whether the emitter's axial position lies above or below the focal plane, we only report the absolute value of the emitters' axial position. As evident from fig. 2c, BNP-Track successfully identifies and localizes the same tracks within the selected ROI in the two parallel camera datasets of ROI-1 despite different noise realizations on each camera and background. Of note, the two square ROI-1's are rotated relative to one another based on careful image registration in post-processing.

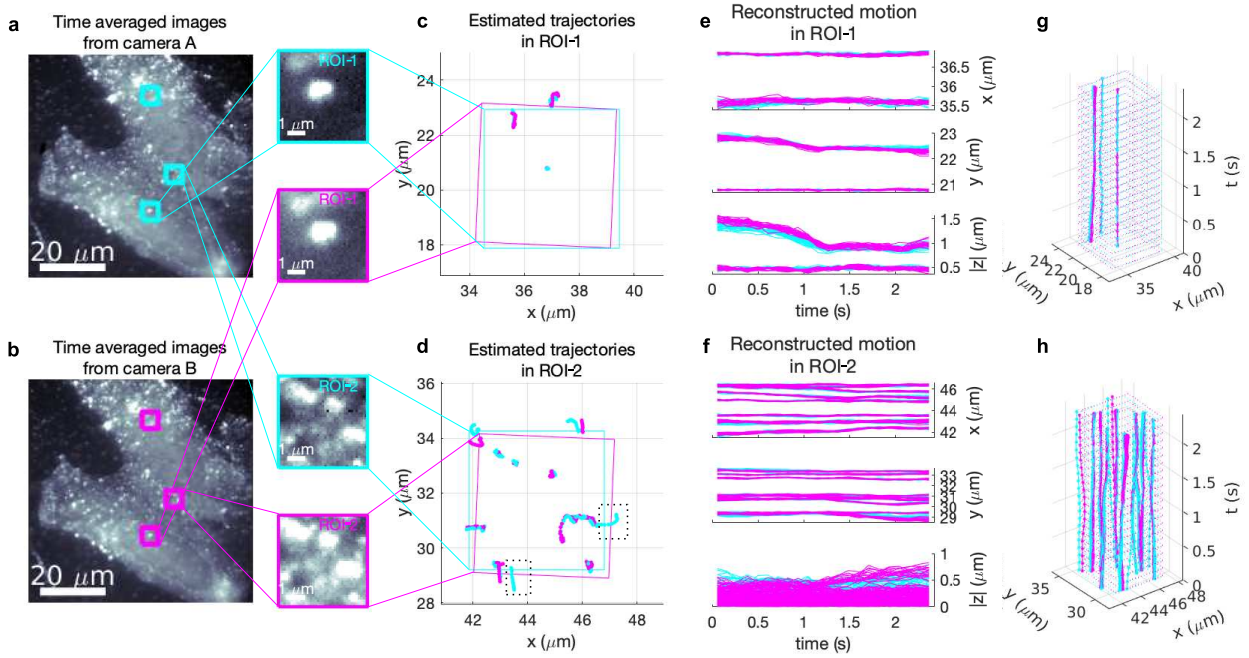

Figure 2: *Testing BNP-Track's performances on two* $5\,\mu$m*-wide regions of interest with different emitter densities based on an experimental dataset from fluorophore-labeled mRNA molecules diffusing in live U-2 OS cells onto a dual-camera microscope.* **a** *and* **b**, *For convenience only, we show time-averages of all 22 frames analyzed from camera A and B, respectively. The selected ROIs are boxed. We zoom in on ROI-1 and ROI-2 in the subpanels. The other ROI, ROI-3, is zoomed in on and analyzed later in the text (fig. 6).* **c** *and* **d**, *Estimated tracks within the selected ROIs from both cameras with solid boxes indicating the corresponding ROIs after image registration.* **e** *and* **f**, *Reconstructed time courses for individual tracks from the selected ROIs. The dotted boxes in* **d** *highlight two emitter tracks only detected by camera A.* **g**, *Time course reconstruction by combining (***e**, *top) and (***e**, *middle).* **h**, *Time course reconstruction by combining (***f**, *top) and (***f**, *middle).*

fig. 2e shows tracks of all well separated emitters identified within this field of view. We note that despite the fact that the center of the PSF of the emitter near the top of ROI-1 in fig. 2c is outside ROI-1 from both cameras for all 22 frames, it is still surprisingly independently picked up in the analysis of the data from both cameras. However we exclude this unique track outside the field of view from fig. 2e and further analysis.

The agreement between tracks across both cameras within their field of view is quantified according to the pairing distance; further details in appendix J.2. This reveals a localization error of $73\,$nm in the lateral direction. Consequently, BNP-Track's average error from the underlying ground truth is one half of the localization error, or about $\approx 37\,$nm, consistent with prior superresolution values [32, 52, 2].

As BNP-Track provides estimates of the lateral as well as the magnitude of the axial emitter position (see details in METHODS), we can also assess the full localization error in 3D. This results in a 3D pairing distance of $97\,$nm and thus a $\approx 48\,$nm localization error from ground truth. Having shown that we can track emitters in a dilute regime similar to ROI-1 of figs. 2c and 2d, we next analyze a more challenging ROI, ROI-2, (figs. 2e and 2f) where emitter PSFs now occasionally overlap.

As before, for illustrative purposes alone, in figs. 2a and 2b we show time averages of a sequence of 22 successive frames spanning $\approx 2.5\,$s of real time. Figures 2e, 2f and 2h reflect the same information described for ROI-1. Also, just as in ROI-1, BNP-Track can track emitters even when they diffuse away from a camera's field of view.

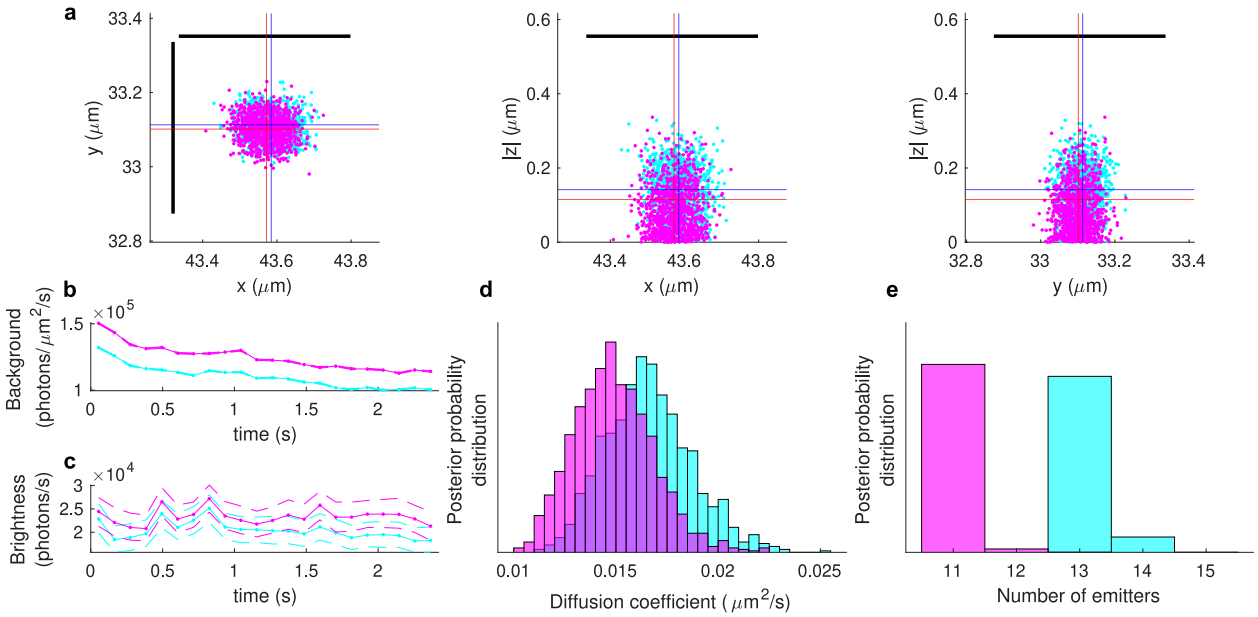

Figure 3: *Testing BNP-Track's performance for ROI-2 of figs. 2e and 2f. The color scheme here is the same as in fig. 2 (cyan for camera A and magenta for camera B).* **a**, *Localization estimates in the lateral and axial directions at a selected frame of a selected emitter. Dots indicate individual positions sampled from the joint posterior distribution (as detailed in* Methods*) and blue and red crosses indicate average values for cyan and magenta, respectively. The black line segments mark the diffraction limit in the lateral direction.* **b** *and* **c**, *Estimated background photon fluxes and emitter brightnesses for both cameras throughout the course of imaging. Dotted lines represent median estimates and dashed lines map the 1%-99% credible interval.* **d** *and* **e**, *The posterior distributions of diffusion coefficient and number of emitters for both cameras.*

Using the pairing distance to quantify the localization error in the lateral direction between the two cameras, for ROI-2 the localization error is slightly higher at 128 nm with an error from the ground truth of about 64 nm, which remains under the nominal diffraction limit of 231 nm. Additionally, the localization error in 3D is now slightly elevated compared to the one from ROI-1, to 159 nm, resulting in the error from ground truth of about 80 nm.

BNP-Track also estimates other dynamical quantities including the background photon fluxes (photon per unit area per unit time), the emitter brightness (photon per unit time), the diffusion coefficient, and the number of emitters. Estimates for these quantities are summarized in fig. 3. It is worth noting that figs. 3b and 3c show that both the system's background flux and emitter brightness vary over time, making ROI-2 more challenging. Despite the agreement between tracks deduced from both cameras below light's diffraction limit, discrepancies in some quantities (such as diffusion coefficient in fig. 3d) highlight the sensitivity of these quantities to small track differences below light's diffraction limit. Similarly, small discrepancies in the emitter brightness estimates (fig. 3c) may be induced by minute dissimilarities in the optical path leading to each camera.

Finally, the number of emitters detected in the two cameras are different (fig. 3e), with the additional tracks detected by camera A highlighted by dotted boxes in fig. 2d. This is unsurprising for three reasons. First, the two cameras have slightly different fields of view. Second, as highlighted by the dotted boxes in fig. 2d, a significant portion of the two extra tracks lie outside the fields of view of either cameras and thus are difficult tracks to detect under any circumstance. Third, as background noise can be mathematically modeled by out-of-focus emitters, and since two cameras draw slightly different conclusions on background photon emission rates and molecular brightnesses (figs. 3b and 3c), this may also naturally lead to slightly different estimates of the number of emitters especially out-of-focus. That is, BNP-Track not only detects in-focus emitters, but uses what it learns from in-

focus emitters to extrapolate outside the field of view or the focal plane. In such regions the number of photons used by BNP-Track to draw inferences on tracks is naturally limited.

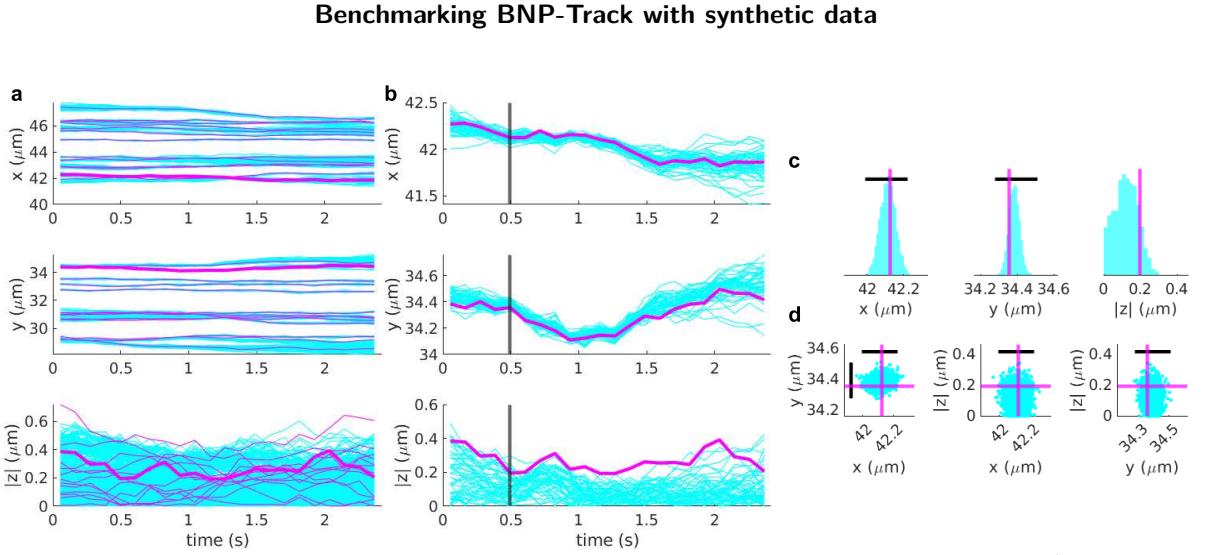

Figure 4: *BNP-Track's performance using synthetic data. Through all panels, BNP-Track's samples are in cyan and ground truths are in magenta.* **a**, *BNP-Track's reconstructions of time courses for all emitters' tracks.* **b**, *The track reconstructions of an out-of-focus emitter. This emitter's ground truth track is highlighted in* **a** *with thicker lines.* **c**, *Posterior distributions of individual localizations corresponding to the time level highlighted in* **b** *with black vertical lines. The black line segments mark the lateral diffraction limit in* **c**. **d**, *Sampled emitter locations in the lateral and axial directions. Again, crosses show estimate means and black line segments mark the lateral diffraction limit.*

We next validate our method using synthetically generated data where the ground truth is known *a priori*. In order to generate realistic data, we start from the estimated tracks of the MAP joint sample of camera A's ROI-2 as our ground truth. We then add optical artifacts and noise according to METHODS. Parameters (NA, pixel size, frame rate) used in the simulations are either identical to those of our experiments or, in the case of brightness and background photon flux, identical to those estimated from experiment (fig. 3).

Figure 4a shows the ground truth in magenta and the estimated tracks in cyan with a unique track highlighted as a wider magenta line. The total pairing distance with ground truth in 2D amounts to a localization error of $76\,\text{nm}$, and in 3D amounts to $145\,\text{nm}$, both remain under the nominal diffraction limit. It is important to note that these numbers are calculated with several out-of-focus emitters included, as shown in fig. 4a bottom panel. Figure 4b focuses on the highlighted magenta track. It is important to note that the selected emitter is out-of-focus as its ground truth axial distance ($|z|$) fluctuates between $200\,\text{nm}$ to $400\,\text{nm}$. To provide a detailed demonstration of BNP-Track's performance, we further quantify the localization at $0.5\,\text{s}$ (indicated by a black vertical line in fig. 4b) in fig. 4c. The lateral and axial localization error determined from the pairing distance with ground truth are shown in fig. 4c, where the lateral localization error is compared to the nominal diffraction limit. We also quantify co-localization in all three spatial directions fig. 4d. Both figs. 4c and 4d show that BNP-Track is capable of beating the diffraction limit even for out-of-focus emitters.

Next, in fig. 5, we test how closely two emitters can come together while retaining BNP-Track's ability to enumerate the number of emitters and track them. To this end, a pair of estimated tracks from ROI-2 of fig. 2 were used as ground truth for the simulation of synthetic data (shown in figs. 5a to 5f) using the same parameters as in fig. 4. Then, the mean displacement between emitters is gradually decreased. Figures 5g to 5l show reconstructed tracks and comparison with the ground truth. Remarkably, the localization error estimated from the total pairing

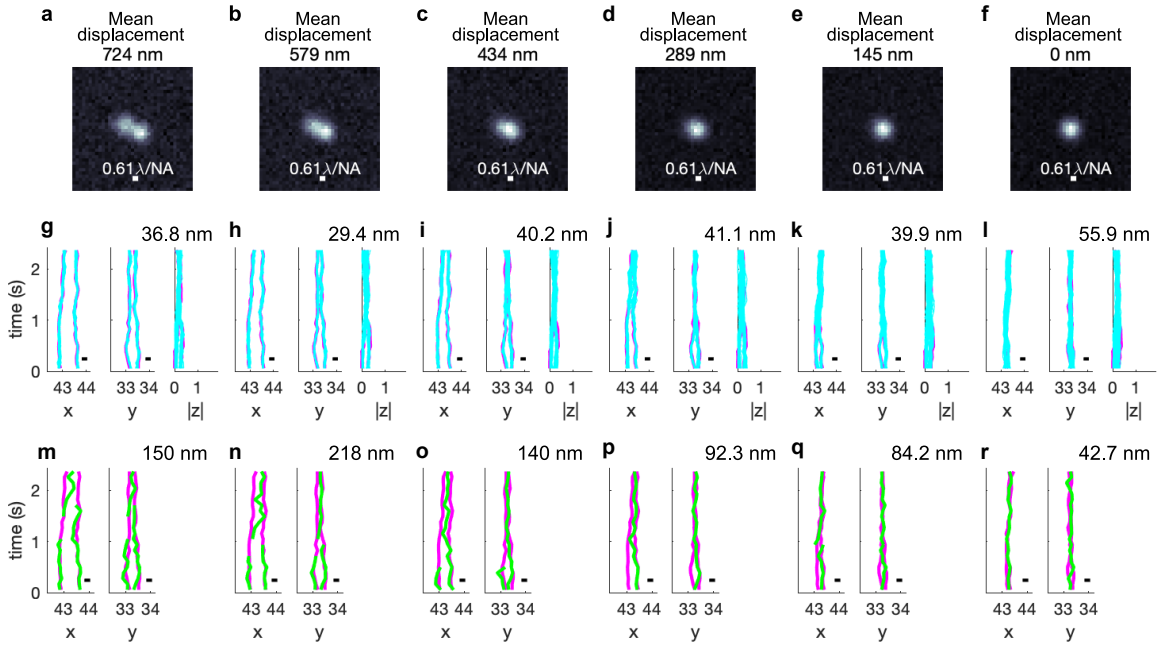

Figure 5: *Benchmarks of BNP-Track on the mean displacement between two tracks. TrackMate tracks are also provided for comparison.* **a**-**f**, *The time-averaged images for the synthetic scenarios. The mean displacements are* $724\,\text{nm}$ *(***a***),* $579\,\text{nm}$ *(***b***),* $434\,\text{nm}$ *(***c***),* $289\,\text{nm}$ *(***d***),* $145\,\text{nm}$ *(***e***), and* $0\,\text{nm}$ *(***f***).* **g**-**l**, *BNP-Track's reconstructed tracks for all coordinates. Reconstructed tracks are in cyan and the ground truths are in magenta. Lateral localization errors are listed at the top right of each panel.* **m**-**r**, *TrackMate's estimated tracks (green) of the same datasets with the ground truths (magenta). Lateral localization errors are listed at the top right of each panel, with missing segments excluded. Also, no axial results are plotted in (***m***-***r***) as TrackMate does not provide axial tracks for 2D images.*

distance remains $\approx 40\,\text{nm}$ in 2D and slightly increases (by $\approx 50\,\text{nm}$) in 3D throughout the synthetic scenarios, below the diffraction limit.

Next, in figs. 5m to 5r, we benchmarked BNP-Track against TrackMate [48] as a well-established single particle tracking software which combines and is built upon contest leading tracking methods [5]. We also show characteristic estimates on the same datasets as figs. 5a to 5f, including comparison against the ground truth using localization errors. In using TrackMate, we note that: (i) The program is manually tuned (for instance, the number of emitters is adjusted to obtain the best matching tracks); and (ii) the lateral localization errors are calculated without taking into account missing segments or whole tracks. Both of these factors provide TrackMate with significant advantages. Even so, we find BNP-Track's localization error to be smaller under most circumstances. Detailed quantitative comparisons generated by the Tacking Performance Measures plugin [5] in Icy [9] are provided in tables A.1 to A.6 and more extensive comparisons are given in a companion manuscript.

It is not unexpected that we find existing tracking methods, such as TrackMate, failing to resolve emitters with separations close to or below the diffraction limit (figs. 5p to 5r). However, TrackMate also misses track segments when the mean lateral displacements between tracks lie well above the diffraction limit (figs. 5m to 5o). Emitter tracks moving out-of-focus contributes to these missing segments. This is most clearly evidenced by noting that in figs. 5a to 5c, one emitter's average intensity is lower and broader. More quantitatively, this is because this emitter, as seen in figs. 5g to 5i, has a $|z|$ position at a distance $200\,\text{nm}$ from the focal plane. In contrast, by leveraging spatiotemporal information, BNP-Track can still track these out-of-focus emitters. In the companion manuscript, we detail this point in greater depth.

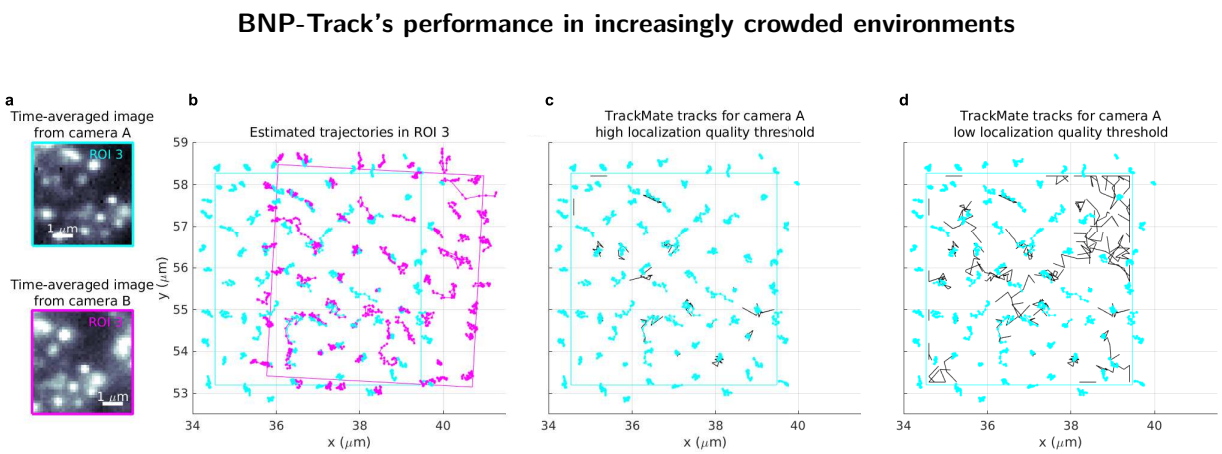

Figure 6: *BNP-Track can track in more crowded environment.* **a**, *Time-averaged images over 22 frames from both cameras show that there are many diffraction-limited emitters within the ROI, ROI-3.* **b**, *BNP-Track's tracking results after registering fields of view.* **c**, *A comparison between BNP-Track's result and TrackMate's result with a high localization quality threshold for the data from camera A. TrackMate tracks are in black; see [48] for the definition of quality.* **d**, *A comparison between BNP-Track's result and TrackMate's result with a low localization quality threshold for the data from camera A. TrackMate tracks are in black.*

So far, we have evaluated the performance of BNP-Track on two distinct ROIs from an experimental dataset and confirmed its resolution using synthetic data. To further test the limits of BNP-Track, we analyzed a densely-packed ROI, ROI-3, selected from the same data set. See figs. 2a and 2b for where ROI-3 lies.

Here in fig. 6a, similar to figs. 2a and 2b, we first present time-averaged images from both cameras. These images reveal that ROI-3 contains tens of closely positioned as well as out-of-focus emitters, as evidenced by the irregular shapes and lower intensities of certain bright regions in fig. 6a. Furthermore, within ROI-3, cameras A and B observe different fields of view, offset by approximately $1.5\,\mu$m and rotated by 5°, thereby introducing additional challenges. To provide an assessment of BNP-Track's performance to compare with TrackMate, we selected the in-focus emitters in the overlapping region and calculated the pairing distance between tracks. We define "in-focus" emitters as emitters whose estimated z position is within $150\,$nm of the in-focus ($z = 0$) plane. The results show a localization error derived from this pairing distance of approximately $136.4\,$nm, which corresponds to a localization error of $68.2\,$nm compared to the ground truth. These results are consistent with the performance for ROI-2 in fig. 2.

As illustrated in figs. 6a and 6b, ROI-3 presents a challenge for emitter number estimation due to crowding which inherently increases the number of out-of-focus emitters in addition to overlapping PSFs. This poses serious issues for conventional tracking tools relying on manually setting thresholds to fix the number of emitters especially dim ones out-of-focus. To demonstrate this point, we again used TrackMate to analyze the dataset from ROI-3. The analysis results for camera A are illustrated in figs. 6c and 6d. Specifically, for fig. 6c we set a relative high localization quality threshold at 5 to minimize spurious detection, resulting in a total of 18 tracks. Each of these tracks can be paired with one of BNP-Track's 78 emitter tracks using the Tracking Performance Measures tool [5] in Icy [9] with the maximum paring distance set at two pixels or $266\,$nm (which is close to the nominal diffraction limit of $231\,$nm). Even with a high localization threshold TrackMate produced significantly fewer emitter tracks than BNP-Track due to out-of-focus dim emitters in addition to overlapping PSFs. In contrast, for fig. 6d, we lowered the quality threshold in TrackMate to 0 to detect more emitters, which increased the total number of TrackMate tracks to 64. Using the same pairing distance threshold, 41 of these tracks can be paired with a subset of BNP-Track's emitter tracks. However, there are also 23 spurious tracks, which contaminate further analyses. These results underscore the importance of inferring the number of emitters simultaneously while tracking rather than determining emitter numbers independently.

Discussion

We present here an image processing framework, BNP-Track, superresolving particles *in cellulo* without the need for complex fluorophore photodynamics. Our framework analyzes continuous image measurements from diffraction-limited light emitters throughout image acquisition. BNP-Track thereby extends the scope of widefield SRM by leveraging spatiotemporal information encoded across frames and pixels. Additionally, BNP-Track unifies many existing approaches to localization microscopy and single-particle tracking and extends beyond them by decoupling image acquisition from image processing by computationally estimating emitter numbers; see fig. 5.

By operating in three interlaced stages (preparation, imaging, processing) existing approaches to widefield SRM estimate locations of individual static emitters with a generally accepted resolution of ≈ 50 nm or less [32, 52, 2]. Such resolution for widefield applications is a significant improvement relative to the diffraction limit of conventional microscopy, ≈ 250 nm. Although our processing framework cannot lift the limitations imposed by optics, nor eliminate the degradation induced by noise, it can significantly extend our ability to estimate emitter numbers and tracks from existing images with uncertainty both for easier in-focus cases and more challenging cases out-of-focus and partly out of the field of view. In particular, because our framework provides full distributions over unknowns, it readily computes error bars (credible intervals) associated with emitter numbers warranted by images (*e.g.*, figs. 3 and 4), localization events for both isolated emitters and emitters closer than light's diffraction limit, and other parameters including diffusion coefficients.

It is well known that any tracking method will face challenges in certain circumstances, such as out-of-focus motion, crowded environments, or camera saturation. In some cases, the available frames may be insufficient for tracking purposes. Although quantifying when BNP-Track fails is highly dependent on the specific circumstance, we contend that its performance can serve as a measure of whether a dataset provides enough information for emitter tracking. As mentioned in the INTRODUCTION and discussed in the companion manuscript, this is because BNP-Track incorporates spatiotemporal information by modeling the entire process from emitter motion to photon detection, thus maximizing the amount of information extracted from frames. If BNP-Track fails to track in a particular system, conventional tracking methods are also very likely to fail, indicating the need for an alternative experimental protocol.

The analysis of a field of view like those shown in RESULTS ($5\,\mu$m $\times$ $5\,\mu$m or about 1500 pixels, and 22 frames) requires about 300 min of computational time on an average laptop computer. The computational cost of our analysis scales linearly with the product of the number of frames, total pixel number, and the total number of emitters. Larger scale applications are within the realm of existing computational capacity; however, algorithmic improvements and computational optimization will be required to speed up execution time. Despite its higher computational cost compared to current single-particle tracking methods, we argue two points. Firstly, as demonstrated in figs. 5 and 6, cheaper conventional tracking methods not only fail to surpass the diffraction limit, but they also do not learn emitter numbers. Yet learning emitter numbers is especially critical in correctly linking emitter locations across frames, especially in crowded environments. Secondly, our method's time of execution is primarily computational wall-time as BNP-Track is unsupervised and largely free from manual tuning. This stands in contrast to methods such as TrackMate used in the generation of figs. 5 and 6 requiring manual tuning and thresholding for proper execution, as detailed more extensively in a companion manuscript and, even so, are limited by diffraction.

While we have focused on the conceptual basis for how to beat the diffraction limit computationally, with more extensive changes to our processing framework, the methods herein can also be adapted to accommodate specialized illumination modalities including TIRF [10] and light-sheet [44], or even multi-color imaging. All of these adaptations are compatible with Bayesian nonparametric tracking, which relies on the joint assessment of three steps characteristic of traditional single-particle tracking (emitter number determination, emitter localization and linking). Along these same lines, in METHODS, we made many common modeling choices and used parameters common in experiments. For example, we used an EMCCD camera model and assumed a Gaussian PSF. Other

choices can be made by simply changing the mathematical form of the camera model or the PSF provided these assume known, pre-calibrated, forms. None of these changes break the conceptual features of BNP-Track.

Similarly, another assumption made in this study is that BNP-Track considers only a Brownian motion model, and one may question its performance when emitters evolve according to alternative motion models. However, throughout RESULTS, we have demonstrated that BNP-Track yields accurate tracking results consistent across two cameras for an experimental dataset with an unknown emitter motion model, despite assuming Brownian motion. This suggests that BNP-Track remains robust under other motion models. We may thus conceive of the Brownian motion model instead as simply providing a reason to invoke Gaussian transition probabilities, following from the central limit theorem, between locations across frames. What is more, if we have reason to believe that a specific motion model is warranted that may not be accommodated by Gaussian transition probabilities, we may also incorporate this change into our framework.

Currently, post-processing tools are frequently utilized to extract useful information from single-particle tracks, such as diffusion coefficients and diffusive states. These tools range from simple approaches, such as mean square displacement, to more complex methods, such as Spot-On [15] and SMAUG [26]. Since our framework produces tracks, these tracks can be analyzed by these tools and our ability to produce full distributions over tracks may also be helpful in estimating errors over post-processed parameters. It is also conceivable that our output could be used as a training set for neural networks [31] or be used to make predictions of molecular tracks in dense environments [11], such as fig. 6, previously considered outside the scope of existing tools.

Taken together, the framework we present is the first proof-of-principle demonstration that computation feasibly achieves superresolution of evolving targets by avoiding the modular approximations of the existing tracking paradigm which has thus far limited tracking to dilute and in-focus samples.

Methods

Image processing

As we demonstrate in RESULTS, our analysis' goal is the determination of the probability distribution termed the posterior, $p(\theta|W)$. In this distribution, we use θ to gather the unknown quantities of interest, for instance emitter tracks and photon emission rates, and W to gather the data under processing, for instance timelapse images. Below we present how this distribution is derived as well as its underlying assumptions.

To facilitate the presentation, we follow a description in two parts. First, we present a detailed formulation of the physical processes involved in the formation of the acquired images necessary in quantitative analysis discussed earlier. This formulation captures microscope optics and camera electronics and can be further modified to accommodate more specialized imaging setups. In the formulation, the unknowns of interest are encoded by parameters. Second, we present the mathematical tools needed to estimate values for such unknown parameters. That is, we address the core challenge in SRM arising from the unknown number of emitters and their associated tracks and, to overcome this challenge specifically, we apply Bayesian nonparametrics. Our approach in the second part is different from likelihood-based approaches, currently employed in localization microscopy, and is ultimately what allows us to relax SRM's photodynamical requirements.

As several of the notions involved in our description are stochastic, for example parameters with unknown values and random emitter dynamics, we use probabilistic descriptions. Although our notation is standard to the statistics community, we provide an introduction more appropriate for a broader audience in the SUPPORTING INFORMATION.

Model description

Our starting point consists of image measurements obtained in a SRM experiment denoted by w_n^p, where subscripts $n = 1, \ldots, N$ indicate the exposures and superscripts $p = 1, \ldots, P$ indicate pixels. For example, w_2^3 denotes the raw image value, typically reported in ADU or counts and stored in TIFF format, measured in pixel 3 during the second exposure. Similarly, $w_2^{1:P}$ denotes every image value (*i.e.*, entire frame) measured during the second exposure. Since the image values are related to the specimen under imaging, our goal from now on is to develop a mathematical model encoding the physical processes relating the specimen under imaging with the acquired measurements.

Noise The recorded images mix electronic signals that depend only stochastically on an average amount of incident photons [42, 28, 18, 16]. For commercially available cameras, the overall relationship, from incident photons to recorded images, is linear and contaminated with multiplicative noise that results from shot noise, amplification and readout. Our formulation below applies to image data acquired with cameras of EMCCD type, as commonly used in superresolution imaging [32, 18], though the expression below can be modified to accommodate other camera types. Here, in our formulation

$$w_n^p | u_n^p \sim \text{Normal}\left(\mu + \xi u_n^p, \upsilon + f\xi^2 u_n^p\right)$$

where u_n^p is the average number of photons incident on pixel p during exposure n. The parameter f is a camera dependent excess noise factor and ξ is the overall gain that combines the effects of quantum efficiency, pre-amplification, amplification and quantization. The values of μ, υ, ξ, and f are specific to the camera that acquires the images of interest and their values can be calibrated as we describe in SUPPORTING INFORMATION.

Pixelization As shot-noise is already captured, u_n^p depends deterministically on the underlying photon flux

$$u_n^p = \int_{t_n^{\min}}^{t_n^{\max}} dt \iint_{x_{\min}^p, y_{\min}^p}^{x_{\max}^p, y_{\max}^p} dxdy\, U(x, y, t)$$

where $t_n^{\min}$, $t_n^{\max}$ mark the integration time of the n^{th} exposure; $x_{\min}^p, x_{\max}^p, y_{\min}^p, y_{\max}^p$ mark the region monitored by pixel p; and $U(x, y, t)$ is the photon flux at position x, y and time t. We detail our spatiotemporal frames of reference in the SUPPORTING INFORMATION.

Optics We model $U(x, y, t)$ as consisting of background $U_{\text{back}}(x, y, t)$ and fluorophore photon contributions, *i.e.*, flux, from every imaged light emitter $U_{\text{fluor}}^m(x, y, t)$. These are additive

$$U(x, y, t) = U_{\text{back}}(x, y, t) + \sum_{m=1}^{B} U_{\text{fluor}}^m(x, y, t).$$

Specifically, for the latter, we consider a total of B emitters that we label with $m = 1, \ldots, B$. Each of our emitters is characterized by a position $X^m(t), Y^m(t), Z^m(t)$, all of which may change through time. Here, we use uppercase letter X, Y, and Z to for random variables and lowercase letter x, y, and z for general variables. Since the total number B of imaged emitters is a critical unknown quantity, in the next section we describe how we modify the flux $U(x, y, t)$ to allow for a varying number of emitters and in the SUPPORTING INFORMATION we describe how this flux is related to $X^m(t), Y^m(t), Z^m(t)$.

Model inference

The quantities that we are interested in estimating, for example the positions $X^{1:B}(t), Y^{1:B}(t), Z^{1:B}(t)$, are unknown variables in the preceding formulation. The total number of such variables depends upon the number of

imaged emitters B, which in SRM remains unknown thereby prohibiting processing of the images under the flux $U(x, y, t)$. Since B has such subtle effect, we modify our formulation to make it compatible with the nonparametric paradigm of Data Analysis that allows for processing under an unspecified number of variables [54, 36, 50, 12, 35].

In particular, following the nonparametric latent feature paradigm [50, 12], we introduce indicator parameters b^m that adopt only values 0 or 1 and recast $U(x, y, t)$ in the form

$$U(x, y, t) = U_{\text{back}}(x, y, t) + \sum_{m=1}^{M} b^m U^m_{\text{fluor}}(x, y, t).$$

Specifically, with the introduction of the indicators, we increase the number of emitters represented in our model from B to a number $M > B$ that may be arbitrarily large. The critical advantage is that now the total number of model emitters M may be set before processing in contrast with the total number of actual emitters B that remains unknown. With this formulation we infer the values of $b^{1:M}$ during processing, simultaneously with the other parameters of interest. This way, we can actively recruit, *i.e.*, $b^m = 1$, or discard, *i.e.*, $b^m = 0$, light emitters consistently avoiding under/overfitting. Following image processing, our analysis recovers the total number of imaged emitters by the sum $B = \sum_{m=1}^{M} b^m$ and the positions of the emitters $X^m(t), Y^m(t), Z^m(t)$ by the estimated positions of those model emitters with $b^m = 1$. However, a side-effect of introducing M is that our analysis results may depend on the particular value chosen. To relax this dependence, we use a specialized nonparametric prior on b^m that we describe in detail in the SUPPORTING INFORMATION. This prior specifically allows for image processing at the formal limit $M \to \infty$.

Our overall formulation also includes additional parameters, for example background photon fluxes and fluorophore brightness, that may or may not be of immediate interest. To provide a flexible computational scheme, that works around both unknowns types, *i.e.*, parametric and nonparametric, and also allows for future extensions, we adopt a Bayesian approach in which we prescribe prior probability distributions on every unknown parameter beyond just the indicators b^m. These priors, combined with the preceding formulation, lead to the posterior probability distribution $p(\theta|w^{1:P}_{1:N})$, where θ gathers every unknown, on which our results rely. We describe the full posterior distribution and its evaluation in the SUPPORTING INFORMATION.

Image acquisition

Experimental timelapse images

Fluorescence timelapse images of U-2 OS cells injected with chemically labeled firefly luciferase mRNAs were acquired simultaneously on two cameras. Cell culture and handling of U-2 OS cells prior to injections were performed as previously described [40]. Firefly luciferase mRNAs were *in vitro* transcribed, capped and polyadenylated, and a variable number of Cy3 dyes were non specifically added to the polyA tail using CLICK chemistry [8]. Cells were injected with a solution of Cy3 labeled mRNAs and Cascade Blue labeled 10 kDa dextran (Invitrogen D1976) using a Femtojet pump and Injectman NI2 micromanipulator (Eppendorf) at 20 hPa for 0.1 s with 20 hPa compensation pressure. Successfully injected cells were identified by the presence of a fluorescent dextran and were imaged 30 minutes post injection. Cells were continuously illuminated with the 532 nm laser in HILO mode, and Cy3 fluorescence was collected using a 60x 1.49 NA oil objective. Images were captured simultaneously on two Andor X-10 EMCCD cameras by using a 50:50 beamsplitter, with a 100 ms exposure time.

Synthetic timelapse images

We acquire the validation and benchmarking data through standard computer simulations. We start from ground truth as specified in the captions of figs. 4 and 5 and then added noise with values we estimated from the experimental timelapse images according to appendix E.

Acknowledgements

We thank NIH NIGMS (R01GM130745) for supporting early efforts in nonparametrics and tracking, NIH NIGMS (R01GM134426) for supporting single photon efforts, and NIH MIRA entitled "Toward high spatiotemporal resolution models of single molecules for *in cellulo applications".*

References

[1] *F. Balzarotti, Y. Eilers, K. C. Gwosch, A. H. Gynnå, V. Westphal, F. D. Stefani, J. Elf, and S. W. Hell. Nanometer resolution imaging and tracking of fluorescent molecules with minimal photon fluxes.* Science, *355(6325):606–612, 2017.*

[2] *E. Betzig, G. H. Patterson, R. Sougrat, O. W. Lindwasser, S. Olenych, J. S. Bonifacino, M. W. Davidson, J. Lippincott-Schwartz, and H. F. Hess. Imaging intracellular fluorescent proteins at nanometer resolution.* Science, *313(5793):1642–1645, 2006.*

[3] *K. Celler, G. P. van Wezel, and J. Willemse. Single particle tracking of dynamically localizing tata complexes in streptomyces coelicolor.* Biochemical and biophysical research communications, *438(1):38–42, 2013.*

[4] *N. Chenouard, I. Bloch, and J.-C. Olivo-Marin. Multiple hypothesis tracking for cluttered biological image sequences.* IEEE transactions on pattern analysis and machine intelligence, *35(11):2736–3750, 2013.*

[5] *N. Chenouard, I. Smal, F. De Chaumont, M. Maška, I. F. Sbalzarini, Y. Gong, J. Cardinale, C. Carthel, S. Coraluppi, M. Winter, et al. Objective comparison of particle tracking methods.* Nat. Methods, *11(3):281–289, 2014.*

[6] *I. I. Cisse, I. Izeddin, S. Z. Causse, L. Boudarene, A. Senecal, L. Muresan, C. Dugast-Darzacq, B. Hajj, M. Dahan, and X. Darzacq. Real-time dynamics of rna polymerase ii clustering in live human cells.* Science, *341(6146):664–667, 2013.*

[7] *S. Coraluppi and C. Carthel. Multi-stage multiple-hypothesis tracking.* J. Adv. Inf. Fusion, *6(1):57–67, 2011.*

[8] *T. C. Custer and N. G. Walter. In vitro labeling strategies for in cellulo fluorescence microscopy of single ribonucleoprotein machines.* Protein Sci., *26(7):1363–1379, 2017.*

[9] *F. De Chaumont, S. Dallongeville, N. Chenouard, N. Hervé, S. Pop, T. Provoost, V. Meas-Yedid, P. Pankajakshan, T. Lecomte, Y. Le Montagner, et al. Icy: an open bioimage informatics platform for extended reproducible research.* Nat. Methods, *9(7):690–696, 2012.*

[10] *K. N. Fish. Total internal reflection fluorescence (tirf) microscopy.* Current protocols in cytometry, *50(1):12–18, 2009.*

[11] *N. Galvanetto, M. T. Ivanović, A. Chowdhury, A. Sottini, M. Nüesch, D. Nettels, R. Best, and B. Schuler. Ultrafast molecular dynamics observed within a dense protein condensate.* bioRxiv, *pages 2022–12, 2022.*

[12] *Z. Ghahramani. Probabilistic machine learning and artificial intelligence.* Nature, *521(7553):452–459, 2015.*

[13] *W. J. Godinez, M. Lampe, R. Eils, B. Müller, and K. Rohr. Tracking multiple particles in fluorescence microscopy images via probabilistic data association. In* 2011 IEEE International Symposium on Biomedical Imaging: From Nano to Macro, *pages 1925–1928. IEEE, 2011.*

[14] *M. G. Gustafsson. Surpassing the lateral resolution limit by a factor of two using structured illumination microscopy.* J. Microsc., *198(2):82–87, 2000.*

[15] *A. S. Hansen, M. Woringer, J. B. Grimm, L. D. Lavis, R. Tjian, and X. Darzacq. Robust model-based analysis of single-particle tracking experiments with spot-on.* Elife, *7:e33125, 2018.*

[16] *K. B. Harpsøe, M. I. Andersen, and P. Kjægaard. Bayesian photon counting with electron-multiplying charge coupled devices (EMCCDs).* Astronomy & Astrophysics, *537:A50, 2012.*

[17] *S. W. Hell and J. Wichmann. Breaking the diffraction resolution limit by stimulated emission: stimulated-emission-depletion fluorescence microscopy.* Opt. Lett., *19(11):780–782, Jun 1994.*

[18] *M. Hirsch, R. J. Wareham, M. L. Martin-Fernandez, M. P. Hobson, and D. J. Rolfe. A stochastic model for electron multiplication charge-coupled devices – from theory to practice.* PLOS ONE, *8(1):1–13, 01 2013.*

[19] *S. J. Holden, T. Pengo, K. L. Meibom, C. Fernandez Fernandez, J. Collier, and S. Manley. High throughput 3d super-resolution microscopy reveals caulobacter crescentus in vivo z-ring organization.* Proceedings of the National Academy of Sciences, *111(12):4566–4571, 2014.*

[20] *M. Husain, T. Boudier, P. Paul-Gilloteaux, I. Casuso, and S. Scheuring. Software for drift compensation, particle tracking and particle analysis of high-speed atomic force microscopy image series.* Journal of Molecular Recognition, *25(5):292–298, 2012.*

[21] *A. P. Jalihal, S. Pitchiaya, L. Xiao, P. Bawa, X. Jiang, K. Bedi, A. Parolia, M. Cieslik, M. Ljungman, A. M. Chinnaiyan, et al. Multivalent proteins rapidly and reversibly phase-separate upon osmotic cell volume change.* Mol. Cell, *79(6):978–990, 2020.*

[22] *A. P. Jalihal, A. Schmidt, G. Gao, S. R. Little, S. Pitchiaya, and N. G. Walter. Hyperosmotic phase separation: Condensates beyond inclusions, granules and organelles.* J. Biol. Chem., *296, 2021.*

[23] *K. Jaqaman, D. Loerke, M. Mettlen, H. Kuwata, S. Grinstein, S. L. Schmid, and G. Danuser. Robust single-particle tracking in live-cell time-lapse sequences.* Nat. Methods, *5(8):695–702, Aug. 2008.*

[24] *S. Jazani, L. W. Xu, I. Sgouralis, D. P. Shepherd, and S. Pressé. Computational proposal for tracking multiple molecules in a multifocus confocal setup.* ACS photonics, *9(7):2489–2498, 2022.*

[25] *R. Jungmann, M. S. Avendaño, J. B. Woehrstein, M. Dai, W. M. Shih, and P. Yin. Multiplexed 3d cellular super-resolution imaging with dna-paint and exchange-paint.* Nat. Methods, *11(3):313–318, 2014.*

[26] *J. D. Karslake, E. D. Donarski, S. A. Shelby, L. M. Demey, V. J. DiRita, S. L. Veatch, and J. S. Biteen. Smaug: Analyzing single-molecule tracks with nonparametric bayesian statistics.* Methods, *193:16–26, 2021.*

[27] *I. M. Khater, I. R. Nabi, and G. Hamarneh. A review of super-resolution single-molecule localization microscopy cluster analysis and quantification methods.* Patterns, *1(3):100038, 2020.*

[28] *Z. Kilic, I. Sgouralis, W. Heo, K. Ishii, T. Tahara, and S. Pressé. Extraction of rapid kinetics from smfret measurements using integrative detectors.* Cell Reports Physical Science, *2(5):100409, 2021.*

[29] *J. Kim, J. Y. Kim, S. Jeon, J. W. Baik, S. H. Cho, and C. Kim. Super-resolution localization photoacoustic microscopy using intrinsic red blood cells as contrast absorbers.* Light: Science & Applications, *8(1):103, 2019.*

[30] *T. A. Klar, S. Jakobs, M. Dyba, A. Egner, and S. W. Hell. Fluorescence microscopy with diffraction resolution barrier broken by stimulated emission.* Proc. Natl. Acad. Sci. U.S.A., *97(15):8206–8210, 2000.*

[31] *P. Kowalek, H. Loch-Olszewska, and J. Szwabiński. Classification of diffusion modes in single-particle tracking data: Feature-based versus deep-learning approach.* Phys. Rev. E, *100(3):032410, 2019.*

[32] *A. Lee, K. Tsekouras, C. Calderon, C. Bustamante, and S. Pressé. Unraveling the thousand word picture: An introduction to super-resolution data analysis.* Chem. Rev., *117(11):7276–7330, 2017.*

[33] *L. Liang, H. Shen, P. De Camilli, and J. S. Duncan. Tracking clathrin coated pits with a multiple hypothesis based method. In* Medical Image Computing and Computer-Assisted Intervention–MICCAI 2010: 13th International Conference, Beijing, China, September 20-24, 2010, Proceedings, Part II 13, *pages 315–322. Springer, 2010.*

[34] *E. Meijering, O. Dzyubachyk, and I. Smal. Methods for cell and particle tracking.* Methods in enzymology, *504:183–200, 2012.*

[35] *P. Müller, F. A. Quintana, A. Jara, and T. Hanson.* Bayesian nonparametric data analysis, *volume 1. Springer, 2015.*

[36] *P. Orbanz and Y. W. Teh. Bayesian nonparametric models.* Encyclopedia of machine learning, *1, 2010.*

[37] *J. Otterstrom, A. Castells-Garcia, C. Vicario, P. A. Gomez-Garcia, M. P. Cosma, and M. Lakadamyali. Super-resolution microscopy reveals how histone tail acetylation affects dna compaction within nucleosomes in vivo.* Nucleic acids research, *47(16):8470–8484, 2019.*

[38] *E. P. Perillo, Y.-L. Liu, K. Huynh, C. Liu, C.-K. Chou, M.-C. Hung, H.-C. Yeh, and A. K. Dunn. Deep and high-resolution three-dimensional tracking of single particles using nonlinear and multiplexed illumination.* Nature Communications, *6(1):7874, 2015.*

[39] *S. Pitchiaya, L. A. Heinicke, T. C. Custer, and N. G. Walter. Single molecule fluorescence approaches shed light on intracellular rnas.* Chem. Rev., *114(6):3224–3265, 2014.*

[40] *S. Pitchiaya, V. Krishnan, T. C. Custer, and N. G. Walter. Dissecting non-coding rna mechanisms in cellulo by single-molecule high-resolution localization and counting.* Methods, *63(2):188–199, 2013.*

[41] *S. Pitchiaya, M. D. Mourao, A. P. Jalihal, L. Xiao, X. Jiang, A. M. Chinnaiyan, S. Schnell, and N. G. Walter. Dynamic recruitment of single rnas to processing bodies depends on rna functionality.* Mol. Cell, *74(3):521–533, 2019.*

[42] *S. Ram, P. Prabhat, J. Chao, E. Sally Ward, and R. J. Ober. High accuracy 3d quantum dot tracking with multifocal plane microscopy for the study of fast intracellular dynamics in live cells.* Biophysical Journal, *95(12):6025–6043, 2008.*

[43] *L. Rayleigh. XXXI. investigations in optics, with special reference to the spectroscope.* The London, Edinburgh, and Dublin Philosophical Magazine and Journal of Science, *8(49):261–274, 1879.*

[44] *E. G. Reynaud, J. Peychl, J. Huisken, and P. Tomancak. Guide to light-sheet microscopy for adventurous biologists.* Nat. Methods, *12(1):30–34, 2015.*

[45] *M. J. Rust, M. Bates, and X. Zhuang. Sub-diffraction-limit imaging by stochastic optical reconstruction microscopy (STORM).* Nat. Methods, *3(10):793–796, 2006.*

[46] *J. Schnitzbauer, M. T. Strauss, T. Schlichthaerle, F. Schueder, and R. Jungmann. Super-resolution microscopy with DNA-PAINT.* Nature protocols, *12(6):1198–1228, 2017.*

[47] *M. Shayegan, R. Tahvildari, K. Metera, L. Kisley, S. W. Michnick, and S. R. Leslie. Probing inhomogeneous diffusion in the microenvironments of phase-separated polymers under confinement.* J. Am. Chem. Soc., *141(19):7751–7757, 2019.*

[48] *J.-Y. Tinevez, N. Perry, J. Schindelin, G. M. Hoopes, G. D. Reynolds, E. Laplantine, S. Y. Bednarek, S. L. Shorte, and K. W. Eliceiri. Trackmate: An open and extensible platform for single-particle tracking.* Methods, *115:80–90, 2017. Image Processing for Biologists.*

[49] *M. Tokunaga, N. Imamoto, and K. Sakata-Sogawa. Highly inclined thin illumination enables clear single-molecule imaging in cells.* Nat. Methods, *5(2):159–161, 2008.*

[50] *R. van de Schoot, S. Depaoli, R. King, B. Kramer, K. Märtens, M. G. Tadesse, M. Vannucci, A. Gelman, D. Veen, J. Willemsen, et al. Bayesian statistics and modelling.* Nature Reviews Methods Primers, *1(1):1–26, 2021.*

[51] *F. J. Verweij, L. Balaj, C. M. Boulanger, D. R. Carter, E. B. Compeer, G. D'angelo, S. El Andaloussi, J. G. Goetz, J. C. Gross, V. Hyenne, et al. The power of imaging to understand extracellular vesicle biology in vivo.* Nat. Methods, *18(9):1013–1026, 2021.*

[52] *L. von Diezmann, Y. Shechtman, and W. Moerner. Three-dimensional localization of single molecules for super-resolution imaging and single-particle tracking.* Chem. Rev., *117(11):7244–7275, 2017.*

[53] *U. von Toussaint. Bayesian inference in physics.* Rev. Mod. Phys., *83:943–999, Sep 2011.*

[54] *L. Wasserman.* All of nonparametric statistics. *Springer Science & Business Media, 2006.*

[55] *N. P. Wells, G. A. Lessard, P. M. Goodwin, M. E. Phipps, P. J. Cutler, D. S. Lidke, B. S. Wilson, and J. H. Werner. Time-resolved three-dimensional molecular tracking in live cells.* Nano letters, *10(11):4732–4737, 2010.*

[56] *N. P. Wells, G. A. Lessard, and J. H. Werner. Confocal, three-dimensional tracking of individual quantum dots in high-background environments.* Analytical chemistry, *80(24):9830–9834, 2008.*

[57] *K. I. Willig, S. O. Rizzoli, V. Westphal, R. Jahn, and S. W. Hell. Sted microscopy reveals that synaptotagmin remains clustered after synaptic vesicle exocytosis.* Nature, *440(7086):935–939, 2006.*

[58] *M. R. Winter, C. Fang, G. Banker, B. Roysam, and A. R. Cohen. Axonal transport analysis using multi-temporal association tracking.* International journal of computational biology and drug design, *5(1):35–48, 2012.*

[59] *L. Yang, Z. Qiu, A. H. Greenaway, and W. Lu. A new framework for particle detection in low-snr fluorescence live-cell images and its application for improved particle tracking.* IEEE transactions on biomedical engineering, *59(7):2040–2050, 2012.*

[60] *Z. Yin, T. Kanade, and M. Chen. Understanding the phase contrast optics to restore artifact-free microscopy images for segmentation.* Medical image analysis, *16(5):1047–1062, 2012.*

[61] *B. Zhang, J. Zerubia, and J.-C. Olivo-Marin. Gaussian approximations of fluorescence microscope point-spread function models.* Applied optics, *46(10):1819–1829, 2007.*